J Geophys (1988) 62:163–174

Journal of Geophysics

A study of diffraction-like events on DEKORP2-S by Kirchhoff theory

W. Kampfmann
Institute of Meteorology and Geophysics, Feldbergstr. 47, D-6000 Frankfurt 1, Federal Republic of Germany

Abstract. A method is described for calculating the seismic response of an arbitrarily shaped interface below a homogeneous medium by the Kirchhoff integral in the time domain. It is shown, by comparison with other numerical techniques, that this method yields accurate results for reflections. The errors in calculating diffractions are tolerable if the distance of the receiver from the shadow boundary of reflection is not too large; this is usually the case in horizontal seismic profiling. The method has been applied to model qualitatively some typical features in record sections of the deep seismic reflection profile DEKORP2-S. This profile is characterized by numerous strongly curved events that are concentrated mainly in two areas of the profile. These signals can be addressed as diffractions from an interpretation of the travel times. Dynamic calculations, however, show that the surprisingly high amplitudes cannot be explained by diffracting elements like fault edges or small-scale inhomogeneities; instead, one has to assume cylindrically or spherically curved reflectors with a radius of at least 4 km. Some possible geological explanations for these structures, like diapiric intrusions or antiformal stacks, are discussed in view of the tectonic evolution of the Central European Variscides.

Key words: Kirchhoff theory – Diffractions – DEKORP2-S

Introduction

Forward modelling of seismic data has become an important tool in interpretation for both seismology and exploration geophysics. From the numerous methods that exist for the calculation of synthetic seismograms, the Kirchhoff-Helmholtz theory has been used in this paper because it is one of the few treatments – besides approaches that are based on the direct numerical solution of the elastodynamic equations – that incorporates the generation of diffractions in laterally strongly heterogeneous media.

Kirchhoff theory has found wide-spread application in reflection seismology since the work of Hilterman (1970). Early formulations of the Kirchhoff theory were based on the assumption of a constant-velocity medium and a constant reflection coefficient (e.g. Trorey, 1970, 1977; Berryhill, 1977). The method has been extended to media with variable velocities and arbitrary reflectivities by Carter and Frazer (1983), Deregowski and Brown (1983) and Frazer and Sen (1985). The accuracy of the high-frequency approximation that is inherent to all these implementations when modelling diffraction amplitudes has recently been discussed by Hutton (1987). Kirchhoff theory has also been used for the migration of seismic data (Schneider, 1978) and for the inversion of common-offset sections (Sullivan and Cohen, 1987).

This paper uses a time-domain formulation of the Kirchhoff integral for two dimensions to calculate the seismic response of an arbitrarily shaped reflector by a superposition of the elementary scattered waves that are radiated from each point of the reflector. The medium above this interface is assumed to have constant velocity or a linear increase in velocity with depth.

The algorithm is tested by comparison with the finite-difference method and the reflectivity method and then applied to model some conspicuous arched events in seismogram sections, on a near-vertical deep seismic reflection profile in southern Germany, that have been explained as diffractions in an earlier interpretation (DEKORP Research Group, 1985).

Formulation of the Kirchhoff method

Theory

The derivation of Kirchhoff theory can be found, for example, in Trorey (1970), Hilterman (1970) or Frazer and Sen (1985). Therefore, only a brief outline of the time-domain formulation of the Kirchhoff integral for computing synthetic seismograms will be given in the following.

We start with the Helmholtz equation for two dimensions

$$V^2 U + k^2 U = 0, \tag{1}$$

where $k = \omega/c$ is the wavenumber, ω the frequency, c the velocity and $V^2 = \partial^2/\partial x^2 + \partial^2/\partial z^2$. Here, U is the Fourier transform of any quantity that solves the acoustic wave equation in a homogeneous medium. This may be the pressure, the x or z component of P or SV displacement, the horizontal displacement in the case of SH waves, or the displacement potential for P or S waves.

Assume two functions F and G, where F satisfies Eq. (1) within a cross-section A, and G is the Green's function of Eq. (1): $V^2 G(r, r_0) + k^2 G(r, r_0) = -4i \cdot \delta(r - r_0)$. Then the Kirchhoff integral states that the value of F, at a point P inside A, is fixed if F and G and their normal derivatives

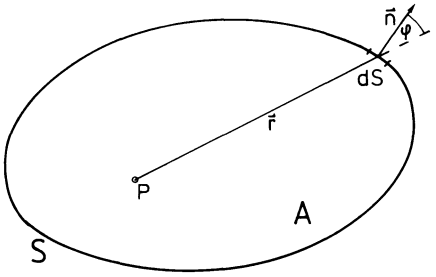

Fig. 1. The area A and its boundary S. $\mathbf{n}$ is the outward unit normal to S. $\mathbf{r}$ is the vector from the receiver at P to the boundary and φ is the angle between $\mathbf{r}$ and $\mathbf{n}$. The wavefield at P can be calculated by integration over S

$\partial F/\partial n$ and $\partial G/\partial n$ are known on the boundary S of A (see Fig. 1):

$$F_P = \frac{i}{4}\cdot\int_S \left(F\frac{\partial G}{\partial n} - G\frac{\partial F}{\partial n}\right) ds \tag{2}$$

($d\mathbf{s} = ds\cdot\mathbf{n}$; $\mathbf{n}$ is the outward-pointing normal unit vector).

Now we identify F with the unknown function U and take G as the Hankel function of the second kind and order zero,

$$G = H_0^{(2)}(kr). \tag{3}$$

In the far field, G takes the asymptotic form

$$G = (2/\pi kr)^{1/2}\exp\left[-i(kr-\pi/4)\right]. \tag{3a}$$

Inserting Eq. (3) into Eq. (2) leads to

$$U_P = -\frac{i}{4}\cdot\int_S \left[U\cdot H_1^{(2)}(kr)k\cos\varphi + H_0^{(2)}(kr)\frac{\partial U}{\partial n}\right] ds \tag{4}$$

(see Fig. 1 for the meaning of r and $\cos\varphi$).

After transformation of Eq. (4) into the time domain, the Kirchhoff formula reads:

$$u_P(t) = \frac{1}{2\pi}\cdot\int_S \left[\frac{\partial u}{\partial t} * \frac{t\cdot H(t-r/c)}{r(t^2-r^2/c^2)^{1/2}}\cos\varphi + \frac{\partial u}{\partial n} * \frac{H(t-r/c)}{(t^2-r^2/c^2)^{1/2}}\right] ds \tag{5}$$

($*$ denotes convolution, $H(t)$ is the Heaviside step function).

To evaluate the wavefield u_P at the point of observation P, we have to know both the time derivative $\partial u/\partial t$ and the normal derivative $\partial u/\partial n$ on the boundary S. These derivatives are retarded by the travel time $T = r/c$ from the boundary to P and low-pass filtered.

In the far-field approximation corresponding to Eq. (3a) we replace the terms t and $t+r/c$ by r/c and $2r/c$, respectively, but keep the differences $t-r/c$. This yields

$$u_P(t) = \frac{1}{2\pi}\cdot\int_S \left[(2rc)^{-1/2}\left(\frac{\partial u}{\partial t}\cos\varphi + \frac{\partial u}{\partial n}\cdot c\right) * \frac{H(t-r/c)}{(t-r/c)^{1/2}}\right] ds. \tag{6}$$

To calculate reflections at some point P above a reflector by means of Eq. (6), we identify the closed boundary S with the reflector and complete it with a half circle with radius R to enclose P. The contribution from the half circle cannot be set to zero as $R\to\infty$ because the term in square brackets of Eq. (6) decays no stronger than $1/R$ and $ds\sim R$. It can be neglected by the argument that this contribution arrives at infinite time.

If the radius of curvature of the reflector is large compared to the dominant wavelength, it is reasonable to approximate the reflected wavefield by use of the reflection coefficient R for plane waves and plane interfaces and the Green's function, Eq. (3a),

$$\begin{aligned} u &= R(\varphi')\cdot\frac{1}{2\pi}\cdot\sqrt{\frac{c}{2r'}}\cdot p(t) \\ &\quad * [H(t-r'/c)/\sqrt{t-r'/c}] \\ &= R(\varphi')\cdot(r^*)^{-1/2}\cdot f(t-r^*/c), \end{aligned} \tag{7}$$

where $p(t)$ is the input wavelet, r' is the distance from the source Q to ds, and r^* the distance from the image source Q^* to ds (Fig. 2). To model a desired output wavelet, it is convenient to define $f(t)$ instead of $p(t)$ in the coding.

Now we can replace $\partial u/\partial n$ and $\partial u/\partial t$ in Eq. (6) by the time derivative $\dot f$ and get (neglecting terms of the order $(r^*)^{-3/2}$ in the far field)

$$\begin{aligned} \frac{\partial u}{\partial n} &\approx R(\varphi')\cdot(r^*)^{-1/2}\cdot\dot f(t-r^*/c)\cdot(-1/c)\cdot\frac{\partial r^*}{\partial n} \\ &= R(\varphi')\cdot(r')^{-1/2}\cdot\dot f(t-r'/c)\cdot\cos\varphi'/c, \end{aligned} \tag{8a}$$

$$\frac{\partial u}{\partial t} = R(\varphi')\cdot(r^*)^{-1/2}\cdot\dot f(t-r^*/c) = R(\varphi')(r')^{-1/2}\cdot\dot f(t-r'/c). \tag{8b}$$

We define

$$g(t) = \dot f(t) * H(t)/\sqrt{t} \tag{9a}$$

and obtain

$$\begin{aligned} &\dot f\left(t-\frac{r'}{c}\right) * \frac{H(t-r/c)}{(t-r/c)^{1/2}} \\ &= g\left(t-\frac{r'+r}{c}\right) = g(t) * \delta\left(t-\frac{r'+r}{c}\right). \end{aligned} \tag{9b}$$

If we insert Eqs. (8) and (9) into Eq. (6), we come finally to an expression that is appropriate for the numerical calculation of synthetic seismograms

$$u_P(t) = g(t)/[2\pi\cdot(2c)^{1/2}] * J(t), \tag{10}$$

with the impulse seismogram

$$J(t) = \int_S \delta\left(t-\frac{r'+r}{c}\right)\cdot R(\varphi')\cdot(r'\cdot r)^{-1/2}\cdot(\cos\varphi+\cos\varphi')\, ds.$$

Equation (10) can be interpreted as a mathematical formulation of Huygens' principle: Each segment ds of the reflector contributes one impulse to the impulse seismogram at the receiver. This impulse is delayed by the proper travel time from the source via ds to P and weighted by the reflection

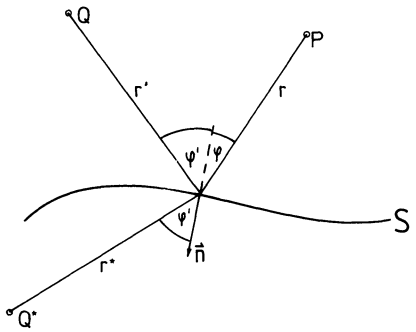

Fig. 2. Source and receiver rays r' and r, and image source ray r^* for a reflector S in a homogeneous medium. Q and P are the positions of source and receiver, Q^* is the image source. **n** is the downward-pointing unit normal vector to S

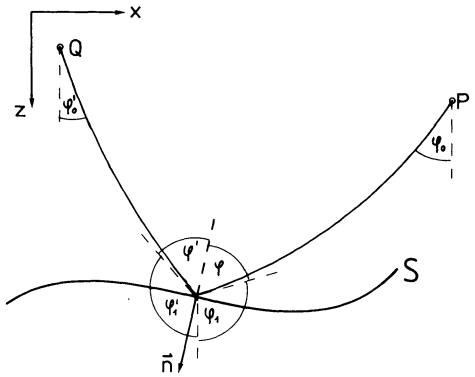

Fig. 4. Ray paths from the source Q to the receiver at P and definition of angles for a reflector below a medium with linear increasing velocity $c=c_0+az$

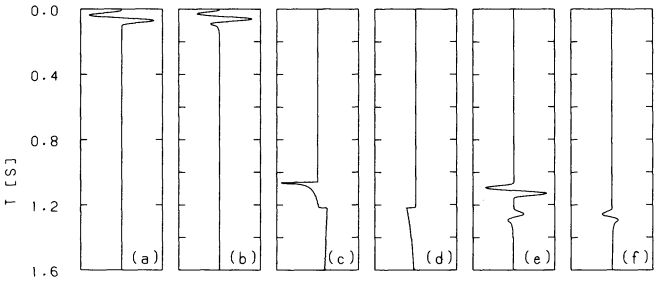

Fig. 3a–f. Example for the different steps in calculating reflections and diffractions from a half-plane by means of Eq. (10). **a** input wavelet $f(t)$; **b** $g(t)$; **c** and **d** impulse seismograms $J(t)$ in the illuminated zone (c) and in the shadow zone (d); **e** and **f** seismograms obtained by convolving c and d with b

coefficient R, the 2-D speading term and the so-called Kirchhoff directivity factor $(\cos\varphi+\cos\varphi')$. The impulse seismogram $J(t)$ is the convolved with the function $g(t)$.

This approach includes the contributions from all parts of the reflector, and the seismogram is built up by constructive or destructive interference of the elementary waves. Hence, the Kirchhoff approach is different from ray theory where only the point of specular reflection generates a response.

It should be noted here that Eq. (10) violates the law of reciprocity in cases where one expects it to hold, e.g. in the case where $u_P(t)$ is the vertical displacement due to a vertical single force. The reason is that exchanging the shotpoint and receiver locations will not keep the reflection coefficient the same in Eq. (10). Some attemps to overcome this defect will be discussed later.

For computational purposes, the interface is approximated by straight reflector elements. The sampling has to be fine enough to avoid diffractions from the endpoints. These elements are further subdivided into integration intervals ds which have to be small compared to the wavelength of the incident wave.

Figure 3 illustrates the different steps of the computation for a reflecting/diffracting half-plane from $x=-\infty$ to $x=0$ km. The source is at $x=0.0$ km and two receivers are placed at $x=-4.2$ km (illuminated zone) and at $x=4.2$ km (shadow zone). The velocity is 5.5 km/s. Figure 3a is the input wavelet $f(t)$ and Fig. 3b follows from 3a by Eq. (9a). Figure 3c and d shows the impulse seismograms $J(t)$ if the receiver lies within the zone of reflection (Fig. 3c) or in the shadow region (Fig. 3d). The reflection arrives at 1.06 s in Fig. 3c and the diffraction arrives in both cases at 1.20 s. Figure 3e and f shows the resulting seismograms obtained by convolving Fig. 3b with Fig. 3c or d. It is evident from Fig. 3c and d that a diffraction changes its sign when the receiver crosses the shadow boundary; this is well known from analytical Kirchhoff diffraction theory (e.g. Hilterman, 1970; Trorey, 1970).

In the case of supercritical reflection ($\varphi'>\varphi_{cr}$), $R(\varphi')$ is complex: $R(\varphi')=R_R(\varphi')+iR_I(\varphi')\cdot\operatorname{sgn}\omega$. In this case the reflection (7) has to be replaced by a linear combination of the input wavelet $f(t)$ and its Hilbert transform $f_H(t)$:

$$u=(r^*)^{-1/2}[R_R(\varphi')\cdot f(t-r^*/c)+R_I(\varphi')\cdot f_H(t-r^*/c)]. \tag{11}$$

The resulting synthetic seismogram is obtained from Eq. (10) by inserting $R_R(\varphi')$ instead of $R(\varphi')$, and adding a similar term that contains $R_I(\varphi')$, and the Hilbert transform $g_H(t)$ instead of $g(t)$. This formulation accounts for the change in the pulse shape with increasing reflection angle $\varphi'>\varphi_{cr}$. It does not include the head wave that will also occur in this case.

The calculation of synthetic seismograms for inhomogeneous media with an equation similar to Eq. (10) requires a large amount of two-point ray tracing to calculate the angles φ and φ' and the travel times T and T' as an equivalent to r/c and r'/c. This has to be done for every integration intervals ds (see Fig. 4 for notation). For this reason, only a special case where the velocity depends linearly on depth, $c=c_0+az$, has been considered here. In this case the ray paths are circular arcs and can be calculated analytically. The far-field approximation of the Green's function takes the following form in analogy to Eq. (3a):

$$G(S,P)=A(S,P)\cdot\left[\frac{2c(P)}{\pi\omega}\right]^{1/2}\exp\left[-i\left(\omega T-\frac{\pi}{4}\right)\right] \tag{12}$$

where $A(S,P)$ is the amplitude at S of a wave that starts from P, and T is the travel time from P to S:

$$A(S,P)=A_0\cdot\left[\frac{\rho(P)\cdot c(P)}{\rho(S)\cdot c(S)}\right]^{1/2}\cdot\left[\frac{l_0^2\cdot\sin\varphi_0}{x\cdot\cos\varphi_1\cdot|\partial x/\partial\varphi_0|}\right]^{1/2} \tag{13}$$

(Müller, 1977), where A_0 is the amplitude at some references distance l_0, ρ is the density and x is the horizontal distance from P to S. For $c=c_0+az$:

$$x=\frac{c_0}{a}\left\{\cot\varphi_0\mp\left[\frac{1}{\sin^2\varphi_0}-\left(\frac{\zeta\cdot a}{c_0}+1\right)^2\right]^{1/2}\right\} \tag{14}$$

where ζ is the vertical distance from P to S,

$$\frac{\partial x}{\partial\varphi_0}=\frac{c_0}{a\cdot\sin^2\varphi_0}$$

$$\cdot\left\{\pm\cot\varphi_0\left[\frac{1}{\sin^2\varphi_0}-\left(\frac{\zeta\cdot a}{c_0}+1\right)^2\right]^{1/2}-1\right\}. \tag{14a}$$

Thus plus sign in Eq. (14) and the minus sign in Eq. (14a) have to be taken if the ray has passed its turning point.

The travel time T is

$$T=\frac{1}{a}\left[\ln\left(\tan\frac{\varphi_1}{2}\right)-\ln\left(\tan\left(\frac{\varphi_0}{2}\right)\right)\right]. \tag{15}$$

Inserting Eq. (12) into Eq. (2) and transforming into the time domain gives finally, in analogy to Eq. (10),

$$u_P(t)=\frac{1}{2\pi\cdot\sqrt{2\cdot c(P)}}\cdot g(t)*J(t)$$

$$J(t)=\int_S\left[\delta(t-(T+T'))\cdot\frac{c(P)}{c(S)}\cdot R(\varphi')\right.$$

$$\left.\cdot A(S,Q)\cdot A(S,P)\cdot(\cos\varphi+\cos\varphi')\right]ds. \tag{16}$$

T' and $A(S, Q)$ correspond to the ray from Q to S (Fig. 4) and are calculated from expressions analogous to Eqs. (15) and (13), respectively.

Numerical tests

As mentioned before, the approximation of the reflected wavefield above the interface with the aid of the reflection coefficient for plane waves and plane interfaces is valid only if the radius of curvature of the reflector is large compared with the wavelength of the incident wave. The applicability of this approximation to strongly curved reflectors and to diffracting structures has to be tested by comparison with exact numerical methods.

The first example is the *SH* reflection from a syncline (Fig. 5a). To avoid supercritical reflection in this case, the S velocities were $v_1=1.5$ km/s and $v_2=1.0$ km/s, and the densities were $\rho_1=2$ g/cm^3 and $\rho_2=1$ g/cm^3. The calculations have been performed for a symmetrical split-spread configuration with the shotpoint above the focus of the syncline. Figure 5c shows the result of a FD calculation (Temme, 1984), and Fig. 5b is the same profile calculated by the Kirchhoff method. The results for the reflections and diffractions from the syncline were practically identical, except for small differences in the amplitudes on the near-focus traces.

This model provided a hard test, because two approximations made in the derivation of Eq. (10) are not strictly fulfilled. Firstly, the average depth to the reflector is about 3 times the dominant wavelength and this is not a typical

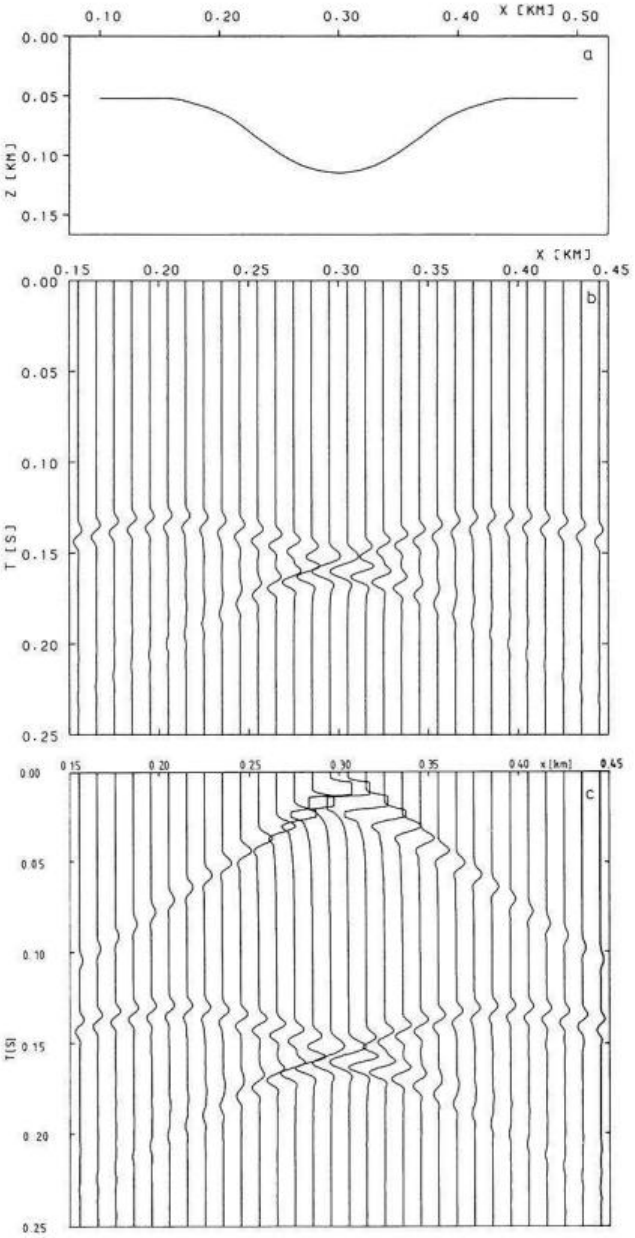

Fig. 5. a Syncline model from Temme (1984), the source is at $x=0.3$ km; **b** Single-shot record, calculated by Kirchhoff theory; **c** Single-shot record, calculated by the finite-difference method (from Temme, 1984)

far-field situation. Secondly, the radius of curvature of the syncline is about 80 m, which is less than 3 times the dominant wavelength and so the assumption of Eq. (7) may not be fully justified for this case. The surprisingly good results indicate that the range of applicability is broader than one might initially expect.

The model of the second example is a reflecting and diffracting edge (Fig. 6a). Figure 6b and c shows the *SH* seismograms for a single shot, calculated by the Kirchhoff (Fig. 6b) and FD methods (Fig. 6c), respectively. The reflection seen between 1.0 and 1.2 s in the left half of the seismogram sections merges with the diffraction at the shadow boundary at $x=1.5$ km. The signal arriving later than 1.7 s in Fig. 6b is a diffraction from the critical point. This phenomenon will be discussed later. The decay of the normal-

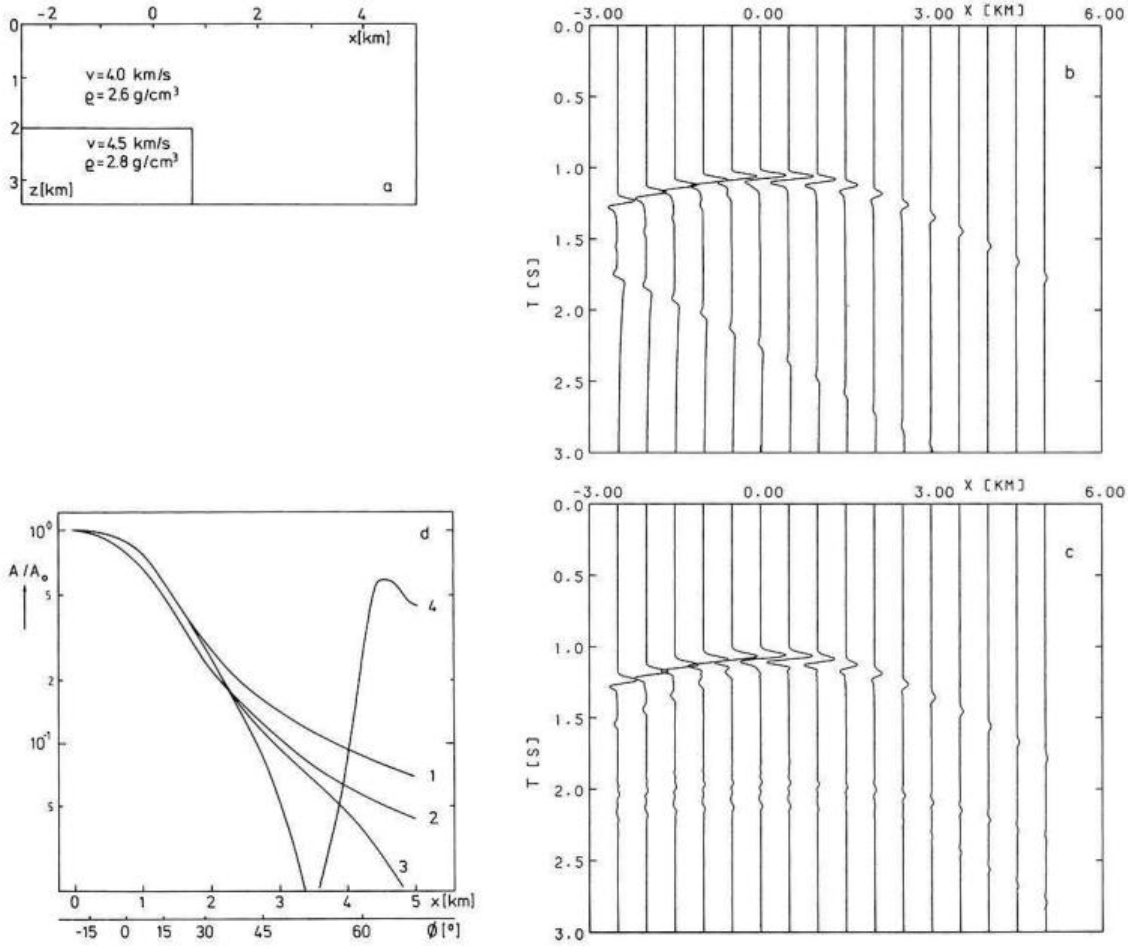

Fig. 6. a Reflecting/diffracting edge in a homogeneous medium, the source is at $x=0$ km; **b** Single-shot record, calculated by Kirchhoff theory; **c** Single-shot record, calculated by the finite-difference method. The events at $T>2$ s are multiple reflections and diffractions, and reflections from the bottom of the model. **d** Normalized reflection/diffraction amplitudes as a function of distance. *1* – Kirchhoff method without reciprocity, $R=R(\varphi')$; *2* – finite-difference method; *3* – Kirchhoff method with reciprocity, $R=R[(\varphi+\varphi')/2]$; *4* – Kirchhoff method with reciprocity, $R=[R(\varphi)+R(\varphi')]/2$. ϕ is the radiation angle from the edge

ized peak-to-peak amplitudes as a function of distance from the diffracting edge is shown in Fig. 6d, lines 1 and 2. For this configuration of source and receivers lying on the same side of the reflecting-diffracting half-plane, Kirchhoff theory gives diffraction amplitudes which are too high compared to the FD method. The errors are tolerable if the radiation angle ϕ at the diffracting edge is not too large, but they reach 50% at $\phi=60°$. They are at least partially caused by the fact that in Kirchhoff theory only the reflected field at the upper side of the reflector is continued upwards, whereas the transmitted field is not considered. The contribution by forward scattering is small at the shadow boundary for reflection, but it increases with increasing distance from the boundary (Fertig and Müller, 1979).

It has been stated above that Eq. (10) violates the law of reciprocity by choosing the reflection coefficient at the angle of incidence φ'. This is of no importance for reflections where $\varphi=\varphi'$, but it may influence diffraction amplitudes. One can enforce reciprocity either by averaging the angles φ and φ' (Deregowski and Brown, 1983) or by averaging the reflection coefficients at φ and φ' (Fertig and Müller, 1979).

Both methods have been tested with the model (Fig. 6d, curves 3 and 4). Calculating the reflection coefficient at $(\varphi+\varphi')/2$ gives better results for small angles, but for larger angles the magnitude of the errors are comparable to those of the unmodified formula (10). Averaging the reflected wavefields yields large errors in the diffraction amplitudes when ϕ approaches the Brewster angle (here 47.6°) or the critical angle (here 62.7°).

The third example demonstrates the validity of the modification of Eq. (10) by use of Eq. (11). The model consists of a 30-km-thick layer over a halfspace. Again *SH* waves are considered. The *S* velocities are 3.5 km/s in the layer and 4.3 km/s in the halfspace, the densities are 2.8 and 3.3 g/cm^3. The Brewster angle, where $R(\varphi')=0$, is reached at a distance $x=61$ km from the shotpoint, and the critical distance is at $x=84$ km. Figure 7a and b shows the seismograms for $x=60$–160 km, as calculated with the Kirchhoff and reflectivity methods.

Both methods yield practically identical results beyond the critical angle, both in absolute amplitude and in pulse shape. The Kirchhoff method produces significant errors in the amplitude near the critical distance (traces 3 and 4 in Fig. 7a). Due to the very rapid variation of the reflection coefficient near the critical angle, the critical point on the interface acts like a diffractor; note arrivals at 10.8 and 10.2 s on traces 1 and 2 of Fig. 7a and the diffraction hyper-

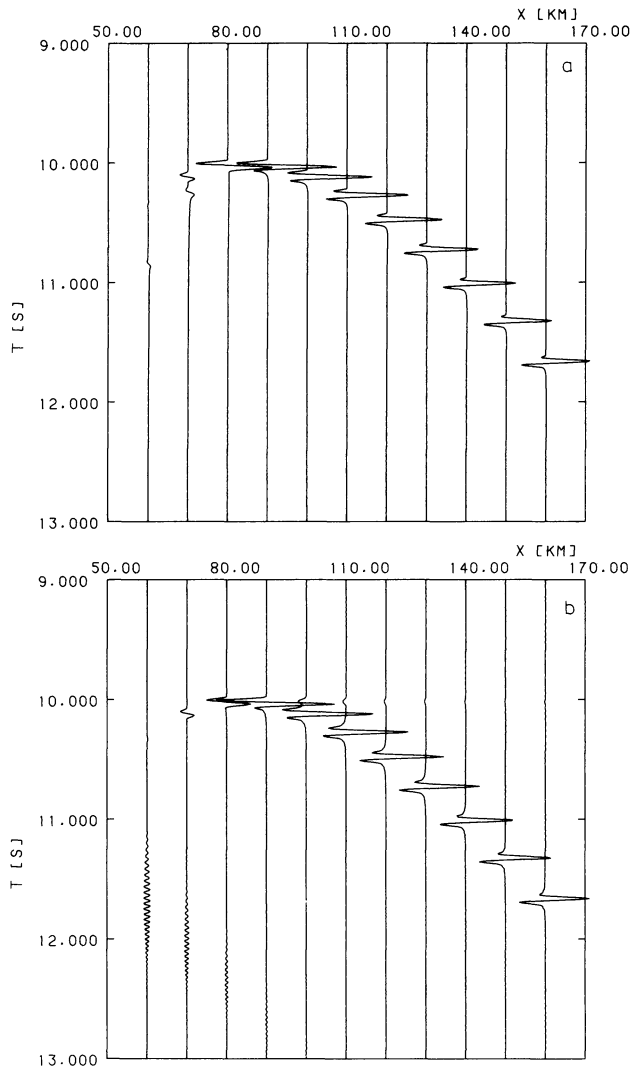

Fig. 7a and b. Single-shot sections for a layer over a halfspace at $z = 30$ km. Time scale is reduced by $v_{red} = 4.3$ km/s. **a** Calculation by Kirchhoff theory; **b** Calculation by the reflectivity method

bola in the left half of Fig. 6b for $t > 1.7$ s. This effect has also been reported by Sen and Frazer (1985). Furthermore, it can be seen in this example that the head wave (weak arrivals at 10 s in Fig. 7b) is not produced by the Kirchhoff method.

These tests show that Kirchhoff theory, in the form presented here, is a reliable method for computing synthetic seismograms for a medium that is bounded at the bottom by an arbitrarily shaped first-order discontinuity. The shortcomings at diffractors and near critical incidence that showed up in the examples must not be taken too seriously, but they should be kept in mind in quantitative interpretations. The computing time depends mainly on the length of the reflector, on the integration interval along this reflector and on the number of receivers per shotpoint. With the model of Fig. 6, the Kirchhoff method was 10 times faster than the FD method. It is an efficient method for simulating recording techniques used in seismic prospecting, such as common-midpoint gathers and zero-offset sections, or even for constructing stacked sections; in these cases, the use of FD methods would often be highly uneconomical. For special problems, the Kirchhoff theory is superior to ray-theoretical methods because diffractions are calculated kinematically and – to a certain degree – are dynamically correct.

The Kirchhoff theory presented here is used for the case of only one reflector. The extension to a multilayered model requires, in general, the evaluation of manifold integrals along each interface in both reflection and transmission. This would make the method highly time consuming. By introducing a generalized interaction coefficient instead of the plane-wave reflection coefficient, Frazer and Sen (1985) could reduce this case to a single-fold path integral.

Application to seismic data

Diffractions on profile DEKORP2-S?

The deep seismic reflection profile DEKORP2-S (Fig. 8) was observed in 1984. An overview of the measurements, the data processing and a preliminary interpretation are given in DEKORP Research Group (1985). The 250-km-long profile extends from SE to NW in southern Germany and crosses the boundaries between the Variscan units Moldanubian, Saxothuringian and Rhenohercynian. Figure 9 shows a line-drawing of the stacked section, corresponding to the southern part of the time profile north of the Ries crater. [See DEKORP Research Group (1985), Figs. 20–25, for a complete representation of the data.]

As in other deep seismic sounding profiles from the European Variscides (e.g. see Matthews and Cheadle, 1986), the upper crust is nearly void of reflections down to about 5 s TWT. By contrast, the lower crust contains many short and sub-horizontal reflections that terminate at the Moho at about 10 s. The upper mantle is again transparent. This part of the profile is dominated by numerous strongly curved events that can be correlated up to 20 km. They are concentrated around km 40 to km 60 and seem to be arranged more or less vertically between 5 and 10 s. A similar cluster of such curved events is also observed in the northern part of the profile below the Spessart mountains (km 150 to 170). These signals were regarded as diffractions in the first interpretation (DEKORP Research Group, 1985).

Diffractions are well known, in reflection seismics, to occur at faults or pinchouts. However, a critical inspection of these arcuate events on the stacked section indicates that they are different from diffractions in mainly two ways. Firstly, they cannot be interpreted as edge diffractions from a reflector that is ending or offset because the accompanying reflection that has to be expected in this case at the apex of the diffraction, is missing here. Secondly, the amplitude of a diffraction reaches a maximum of half the reflection amplitude at the shadow boundary of reflection and decreases very rapidly as the distance from this point increases (see Fig. 6). By contrast, the curved events on the DEKORP2-S profile are the dominating signals of the section and can be correlated over much longer distances than the sub-horizontal reflections from the lower crust.

For a more detailed investigation, common-shot gathers with diffractions have been studied. Figure 10 shows a shot record from the same region that is represented in Fig. 9. No manipulation like AGC, a time-dependent gain function, or trace equalization has been applied. Some prominent reflection events have been marked by *R*, and diffractions by *D*. The interpretation of these latter events as dif-

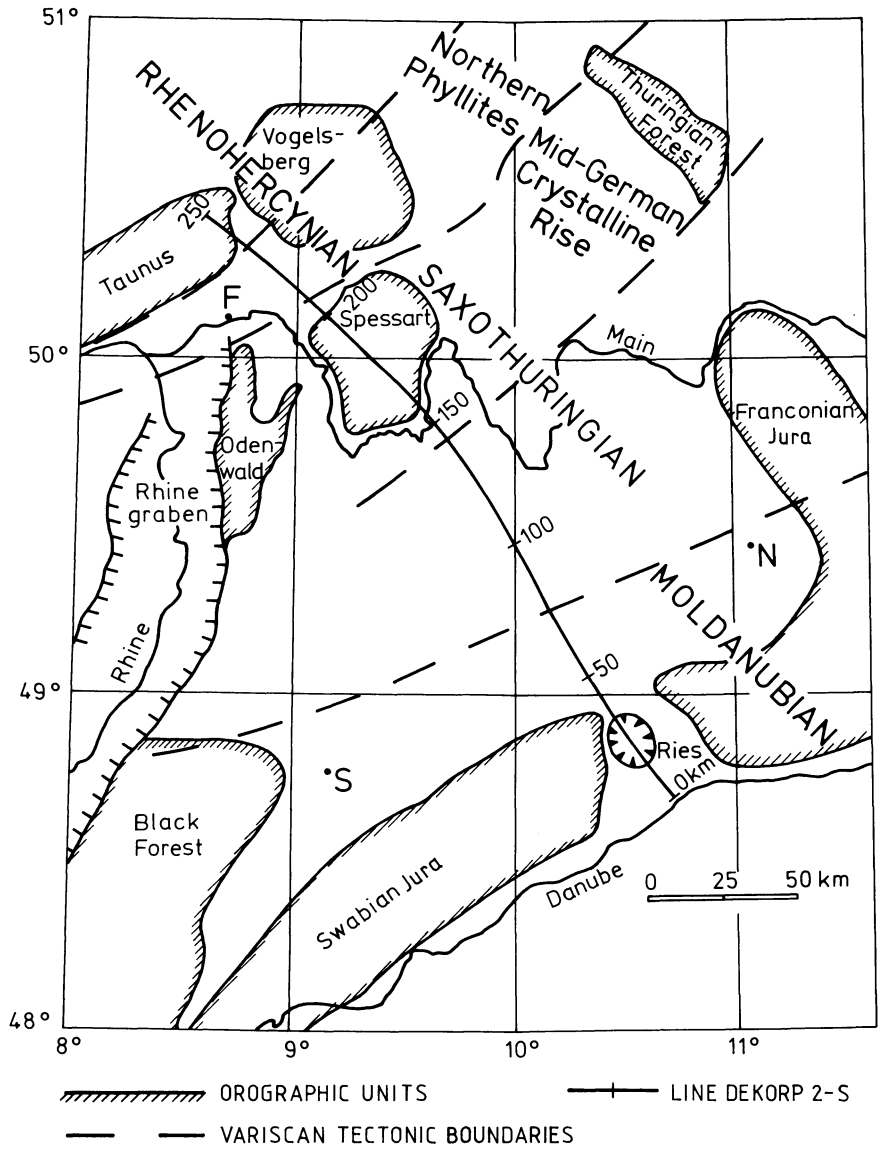

Fig. 8. Location map of the DEKORP2-S profile. *F* – Frankfurt; *S* – Stuttgart; *N* – Nürnberg

fractions follows from a kinematic analysis as demonstrated by Fig. 11. The same event was picked on three different shot records and an attempt was made – after static correction – to fit a diffraction travel-time curve to the three groups of data points. One single point diffractor located at km 55 and at a depth of about 16 km can explain the data very well, even at large offsets. Thus, from travel times alone the diffraction interpretation is well founded. However, it is evident from Fig. 10 that the amplitudes of the so-called diffractions are at least comparable to those of the reflections and that they show no significant decrease in amplitudes along the spread. This is in disagreement with diffraction theory.

Therefore, the diffraction interpretation should be questioned and one should look for alternative subsurface structures. A hint as to where to look comes from the observation that the kinematic analysis yields a rms velocity of 6.4 km/s at 5.5 s TWT, which exceeds the optimum stacking velocity derived from the reflections by almost 20%. Schilt et al. (1981) have reported a similar discrepancy between velocities derived from a diffraction analysis on stacked sections and refraction data in Hardeman County, Texas. They explain these differences by assuming dome models with a radius of several kilometres instead of point diffractors and have used the velocity differences to estimate their radii. Spherical inhomogeneities lead to over-estimates of the velocity when interpreted as point diffractors on a stacked section, but not on single-shot records, as will be seen later.

Model calculations

Forward modelling of amplitudes can possibly give clearer hints about the nature of the structures responsible for the arcuate events than a purely kinematic analysis.

The amplitudes of a line diffractor and different cylindrically curved reflectors (Fig. 12) have been calculated for a single-shot configuration similar to that of Fig. 10 and have been compared with those of a horizontal reflector with the same impedance contrast. The seismograms have been calculated for the vertical component of the *PP* reflection; the velocity and density contrasts are indicated on Fig. 12. The dominant wavelength of the direct wave is 500 m. Figure 13 shows two examples for these calculations: Fig. 13a is the seismogram section for a line diffractor at $x=0$ km

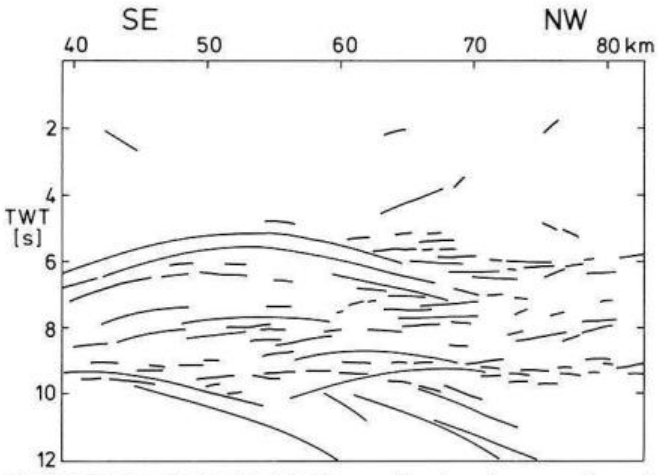

Fig. 9. DEKORP2-S, Dinkelsbühl area; line-drawing, not migrated

and $z=14$ km; Fig. 13b is that of a curved reflector with a radius of curvature of 2 km, i.e. 4 times the dominant wavelength. The centre of curvature is also located at $x=0$ km and $z=14$ km. The source is positioned at the leftmost trace in both cases. The sections have been normalized for plotting purposes, but the amplitudes of the curved reflector exceed those of the diffractor by a factor of 3. It should be noted that the line diffractor in this example is modelled by a strip of half a wavelength width, and not by an edge as in Fig. 6. Consequently, no phase reversal can be observed in this case.

Figure 13c shows the relative amplitudes along the spread for a horizontal reflector, an edge diffractor, a line diffractor and several curved reflectors with different radii of curvature (given in units of the dominant wavelength). They have been normalized to the vertically incident reflection and, hence, they do not depend significantly on the special velocity and density model. The amplitudes of the strip diffractor (which is, of course, a geologically unreasonable model) are only about 10% of the reflection amplitudes along the whole spread. The amplitudes of the edge diffractor decay very rapidly; they fall to about 50% of the reflection amplitude at the shadow boundary ($x=3$ km), as one expects, and coincide with the curve for the line diffractor at larger offsets. The amplitudes of the curved reflectors fall between the curves of the diffractor and the horizontal reflector, and they also show only a weak dependence on offset. The maximum amplitudes of the diffraction-like events D_1–D_3 in Fig. 10 are comparable to those of the reflections. They decrease by a factor of about 3 along the spread and not by a factor of 10 or more as the diffraction in Fig. 13c. It follows, therefore, that structures with a radius of at least 6–10 times the dominant wavelength are required to explain these comparatively big amplitudes of the curved events in the data.

The response of curved reflectors of this size can certainly not be called a diffraction because their dimensions are significantly greater than the Fresnel zone, which has a radi-

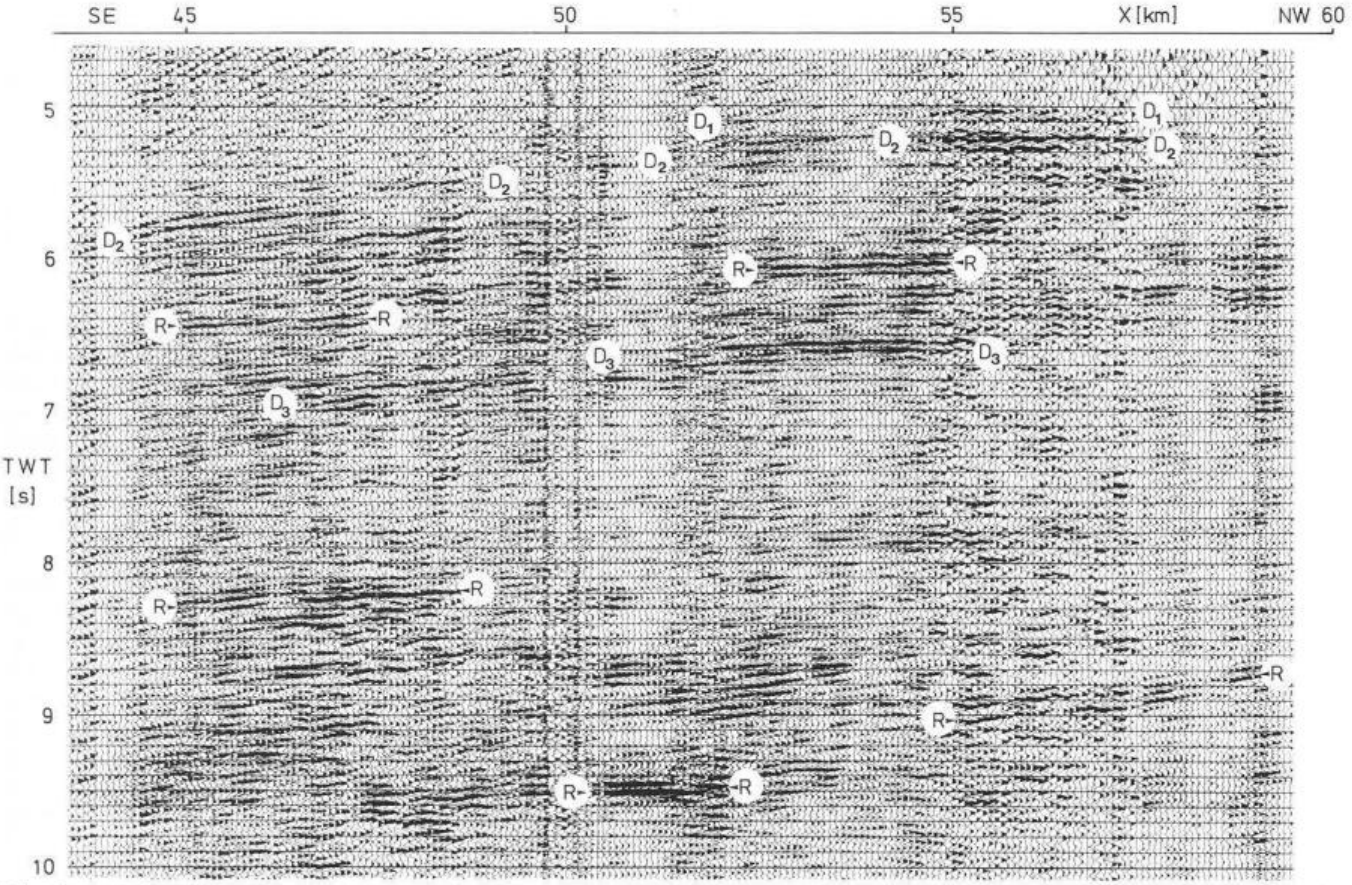

Fig. 10. DEKORP2-S, Dinkelsbühl area; single-shot record (SP 844). R – reflections; D_1–D_3 – diffraction-like events. The shotpoint is at the NW end of the section

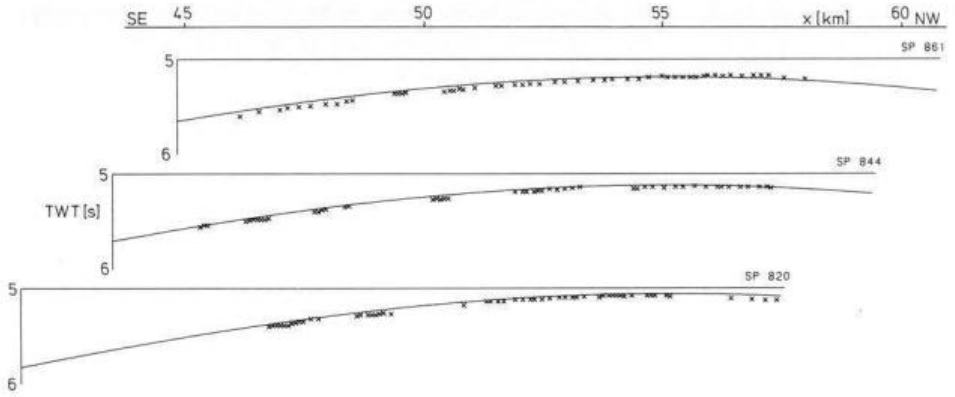

Fig. 11. *Crosses*: arrival times of a diffraction-like event on three shot records. The shot is at the NW end of the spread; the sections are plotted according to their relative position on the profile.
Solid lines: travel-time curves for a point diffractor model at $x = 55.1$ km, $z = 16.1$ km and $v_{rms} = 6.4$ km/s

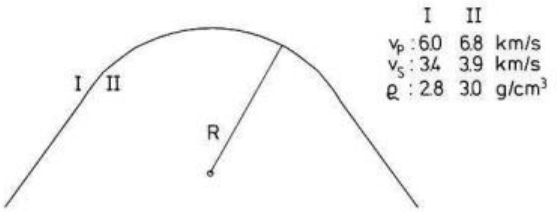

Fig. 12. Diapir-shaped model used for the amplitude calculations of Fig. 13. Depth of centre is $z = 14$ km

us of 1.8 km and, hence, 3–4 wavelengths at this depth [$r_F = (\lambda z/2)^{1/2}$]. Yet, by a purely kinematical analysis these events would be interpreted as diffractions, as can be seen from Fig. 13d. The travel-time curves of the bow-shaped reflectors (solid lines) are practically identical to those of diffractors positioned just at the top of the structures in a medium with the correct velocity, 6.0 km/s. The discrepancies reach a maximum of half a period for $R = 10\lambda$ and large offsets (Fig. 13d, dashed line) and they could easily be explained in real data by residual statics or slight lateral velocity variations.

By contrast to the single-shot records, a travel-time analysis on a zero-offset section would lead to velocities which are systematically too high as already shown by Schilt et al. (1981). For example, a zero-offset section over the reflector with $R = 4\lambda$ (when interpreted with the line diffractor model) gives an erronenous velocity of about 6.3 km/s. The high velocities obtained by a diffraction analysis on single shots from the DEKORP profile (see Fig. 11) cannot yet be explained satisfactorily.

These considerations indicate that the conspicuous curved events, which dominate large parts of profile DEKORP2-S between 5 and 10 s TWT, are not simply diffractions in the usual sense. They can be better explained by strongly curved interfaces in the middle or lower crust. Assuming a velocity of about 6 km/s and a dominant signal frequency of 15–20 Hz for the measurements (DEKORP Research Group, 1985), their radii of curvature can be estimated with the amplitude arguments (see Fig. 13c) to be at least 3–4 km.

One might think that the discrimination between "diffraction" and "reflection" is purely academic in this context. However, once a curved event has been considered as a diffraction, it is often used to obtain velocity information from it. Consequently, a migration process is judged on how good it contracts these events and, hence, structures with similar kinematic characteristics to those proposed here may get lost in a subsequent interpretation.

Geological implications

Qualitative forward modelling of certain aspects of one seismic line can certainly not supply a sufficient basis for a detailed interpretation, but it may allow a discussion of the possible origins of this unusual seismic character.

As mentioned previously, the so-called diffraction clusters are concentrated mainly in two regions along profile DEKORP2-S: one south of the boundary between the Saxothuringian and the Moldanubian, and the other in the Mid-German Crystalline Rise (profile km 160 to 180). They are rather uniformly distributed in a limited time interval. Both observations imply that the geological structures responsible for these events are either aligned vertically, or – if one takes three-dimensional effects into account – that they are arranged along a band that strikes approximately normal to the seismic line, i.e. parallel to the Variscan tectonic boundaries.

This seismic pattern can be generated by different geological structures (see also Schilt et al., 1981), for example:

A. Igneous intrusions in tectonically active regions
B. Antiformal stacks or duplex structures in regions of compressional thrust tectonics
C. Undulated or strongly folded interfaces
D. Combinations or intermediate stages of these examples

Diffractions generated at faults are caused by an abrupt change in impedance contrast at the end of a reflector. Consequently, they should occur at the termination of a reflection signal. Moreover, their amplitudes decay very rapidly with increasing distance from the edge. There is no evidence for these effects in the data.

Synthetic zero-offset seismograms for a three-dimensional undulated interface have been calculated by Blundell and Raynaud (1986). Their section is qualitatively similar to the stacked DEKORP2-S data in showing many criss-crossing curved events over a certain span of time. But the concentrated appearance of these signals along the profile would require such undulated surfaces to occur only in rather narrow zones with no continuation outside.

The first two examples seem to be more likely candidates for an explanation of the so-called diffractions if one regards the tectonic evolution of the European Variscides. An overview of the Variscan orogenesis in Central Europe is given, for example, by Behr et al. (1984) and Weber (1984), and will therefore only be briefly summarized here.

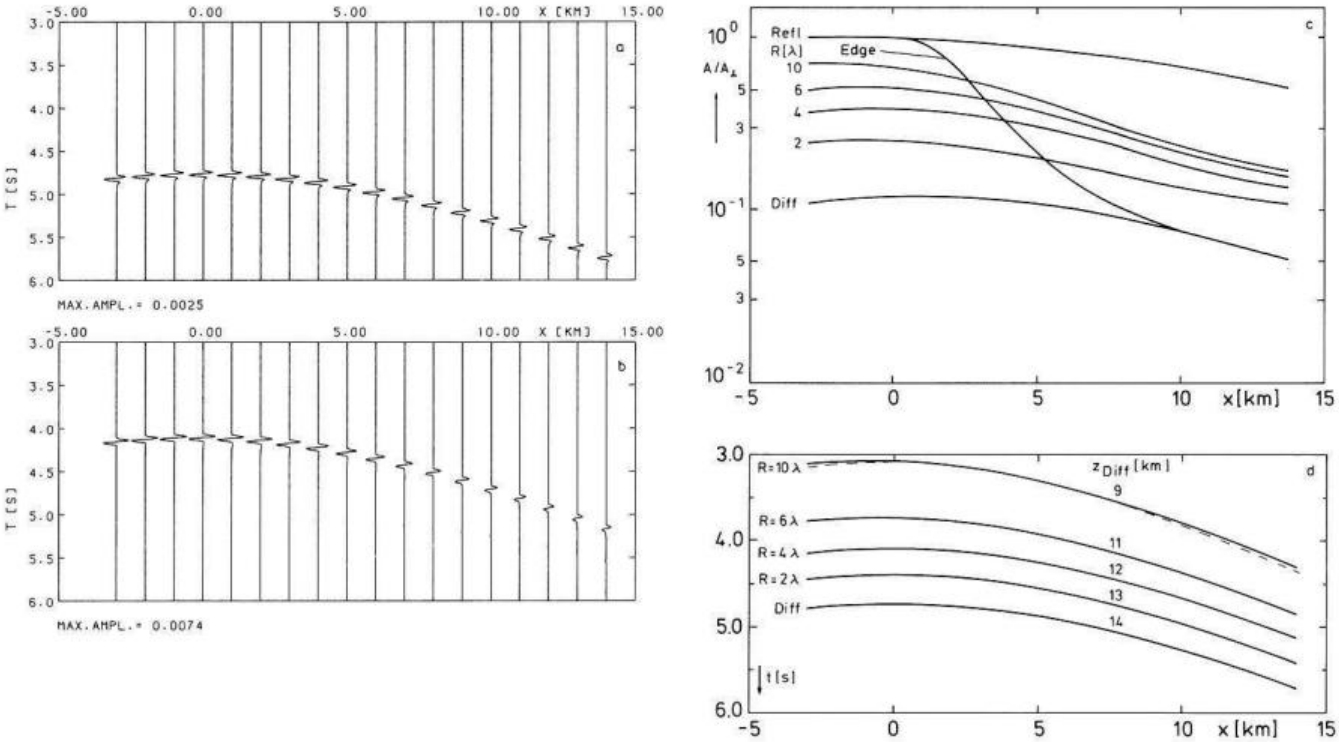

Fig. 13. a Response of a line diffractor at $x=0$ km and $z=14$ km. Model parameters as in Fig. 12; **b** Response of a curved reflector with $R=4\lambda=2$ km. Centre of structure at $x=0$ km, $z=14$ km. The source is at $x=-3$ km in both cases; **c** Normalized amplitudes of different models as a function of distance. *Refl* – horizontal reflector; *Edge* – horizontal half-plane; *Diffd* – line diffractor. The *figures* indicate the radius R of different curved reflector models in units of the wavelength ($\lambda=500$ m); **d** *Solid lines*: travel-time curves of a diffractor and of several curved reflectors as picked from seismogram sections like *a* and *b*. *Numbers* labelled z_{Diff} indicate the depth of a point diffractor with approximately the same travel-time curve. Maximum discrepancy between both models is given by the *dashed line* for $R=10\lambda$

A rifting phase in the early Paleozoic led to the intrusion of granitic melts into the crust and to the formation of sedimentary basins. This extensional process was followed by compression and crustal shortening in a SE-NW direction from the Lower Devonian to the Upper Carboniferous. A period of folding and medium-pressure high-temperature metamorphism of the early Paleozoic rocks and a subsequent uplift and cooling changed with continuing compression into a more brittle deformation regime. This is indicated by the formation of nappes with a NE transport direction, like the Münchberg Massif in the Saxothuringian of Eastern Bavaria, and by the occurrence of mylonite zones at the northern margin of the Mid-German Crystalline Rise and along the boundary between the Saxothuringian and the Moldanubian in the northern Black Forest and at the Erbendorf line at the western margin of the Bohemian Massif. These zones are probably the surficial indications of deep-reaching SE-dipping fault zones. According to the concept of horizontal thrust and nappe tectonics, the Mid-German Crystalline Rise is thrust northward upon the Northern Phyllites and the Moldanubian has been pushed into the Saxothuringian.

Syn- and late-orogenic granites that are now exposed in the Black Forest, the Odenwald, the Fichtelgebirge and south of the Erbendorf line suggest the intercalation of extensional phases. The Variscan orogenesis ended in the Lower Permian with eruptions of rhyolites and melaphyres, which again indicate the transition to a dilatational stress regime.

This geotectonic environment offers several possibilities for the nature of the structures responsible for the diffraction-like pattern of the seismic observations. Both event clusters lie in or near one of the major SE-dipping fault zones. The SE-dipping reflections between 60 and 80 km and between 2 and 4 s in Fig. 9 can probably be seen in connection with the boundary between the Saxothuringian and the Moldanubian.

Deformation processes at the ramps of these thrust systems may have created horses, antiformal stacks or imbricate zones which should strike approximately parallel to the tectonic boundaries. Such highly inhomogeneous zones can give rise to the complicated seismic pattern if their internal structure provides sufficient impedance contrast.

Diapir-like intrusions, also, can not be excluded. Following the strike of the tectonic boundaries, syn- and late-orogenic granites and/or post-orogenic rhyolites are found to the NE as well as to the SW of both event clusters, e.g. in the Saxothuringian in the Odenwald and the Thuringian Forest, and at the boundary to the Moldanubian in the Black Forest, the Fichtelgebirge and the Oberpfalz.

Igneous intrusions have, in general, no internal structure that could be detected by seismic methods. The approximately vertical alignment of overlapping curved events in the time sections would, in this case, be better explained by a linear arrangement of such bodies with a strike more or less normal to the seismic line. The gravity map of southern Germany (see DEKORP Research Group, 1985, Fig. 5) shows two NE-striking chains of Bouguer minima with am-

plitudes of about 10–20 mGal that cross the profile just at the event clusters. Setto and Meissner (1986) have modelled a 2-D gravity profile along the seismic line by introducing there low-density bodies in the lower crust. This interpretation seems to support the assumption of igneous intrusions. However, the gravity map of southern Germany (DEKORP Research Group, 1985, Fig. 5) suggests that a three-dimensional interpretation is necessary. It is questionable whether the accuracy of the gravity data that are available at present could resolve such small anomalies. For example, a spherical body with a radius of 4 km buried at a depth of 15–20 km and with a density contrast of 0.25 g/cm^3 would result in a gravity anomaly of only 1–2 mGal and a half-width of 25–30 km. The gravity pattern may simply reflect the coarse structure of the basement (Edel, 1982) or the NE-striking Permo-Carboniferous troughs in southern Germany.

By using the shotpoints of profile DEKORP2-S and a stationary group of 108 receivers perpendicular to the seismic line at $x=40$ km, a profile P1 could be constructed that runs parallel to the main line at 5 km distance to the east from $x=20$ km to $x=72$ km (DEKORP Research Group, 1985). This profile shows similar clusters of curved events, as in the main profile. When the traces of P1 are plotted at the common midpoints, these clusters seem to be offset to the SE by several kilometres relative to the main profile, but some prominent groups of curved events can still be correlated (DEKORP Research Group, 1985, Fig. 31). However, the close distance between the two profiles does not allow discrimination between the two models proposed here; namely, linear structures like antiformal stacks or diapiric intrusions with a diameter of several kilometres.

Conclusions and discussions

It has been shown that Kirchhoff theory is a valuable and efficient tool in calculating the response of an arbitrarily shaped reflector. It is faster than the finite-difference method and it is, for the purpose of this study, superior to ray-theoretical algorithms because it also includes the generation of diffractions.

This method has been applied to examine some strong diffraction-like events on a deep seismic reflection profile in southern Germany. In order to model the amplitudes of these signals, at least qualitatively, it was necessary to investigate single-shot records because the amplitudes of a stacked section are too strongly distorted by the processing steps involved in stacking. Synthetic seismograms for several dome-shaped models demonstrated that a simple diffractor hypothesis is not able to explain the surprisingly big amplitudes of these arched signals. Instead, one has to assume larger structures in the middle or lower crust with a radius of curvature of at least 3–4 km. Due to the similar travel-time curves of such strongly curved reflectors and diffractors, this result could not have been obtained by a purely kinematic analysis alone.

Whether these structures have approximately spherical upper surfaces, like diapirs, or a mostly two-dimensional geometry, like antiformal stacks, cannot be decided on the basis of the data available.

Two-dimensional theory has been applied to data from a 3-D real world in this study. The difference in the spreading terms ($1/\sqrt{r}$ vs. $1/r$) is not critical and, moreover, it mainly cancels by comparing signals with approximately equal travel times. One should expect, in 3-D theory, slightly different amplitude ratios between the response of a horizontal reflector, diapir-shaped models and point diffractors. In this case the models may have a finite radius of curvature in both x and y directions, and, hence, their defocussing effect will be greater. But this would not affect the main arguments outlined above.

Acknowledgements. This study was financed by the German Ministry of Research and Technology under contract number RG 8702. I am greatly indebted to G. Müller for his help and for many discussions on the subject of this paper. The single-shot data have been provided by the DEKORP Processing Centre, Clausthal, and plotted by Preussag AG, Hannover. I also thank I. Hörnchen for her efficient typing of the manuscript.

References

Behr, H.-J., Engel, W., Franke, W., Giese, P., Weber, K.: The Variscan Belt in Central Europe: main structures, geodynamic implications, open questions. Tectonophysics **109**, 15–49, 1984

Berryhill, J.R.: Diffraction response for nonzero separation of source and receiver. Geophysics **42**(6), 1158–1176, 1977

Blundell, D.J., Raynaud, B.: Modeling lower crust reflections observed on BIRPS profiles. In: Reflection seismology: a global perspective, Barazangi, M., Brown, L., eds.: pp. 287–295. AGU Geodynamics Series, Vol. 13, Washington D.C., 1986

Carter, J.A., Frazer, L.N.: A method for modeling reflection data from media with lateral velocity changes. J. Geophys. Res. **88**, 6469–6476, 1983

DEKORP Research Group: First results and preliminary interpretation of deep-reflection seismic recordings along profile DEKORP2-South. J. Geophys. **57**, 137–163, 1985

Deregowski, S.M., Brown, S.M.: A theory of acoustic diffractors applied to 2-D models. Geophys. Prosp. **31**, 293–333, 1983

Edel, J.B.: Le socle varisque de l'Europe moyenne apports du magnétisme et de la gravimétrie. Sci. Géol. Bull. **35**, 207–224, 1982

Fertig, J., Müller, G.: Approximate diffraction theory for transparent half-planes with application to seismic-wave diffraction at coal seams. J. Geophys. **46**, 349–367, 1979

Frazer, L.N., Sen, M.K.: Kirchhoff-Helmholtz reflection seismograms in a laterally inhomogeneous multi-layered elastic medium – I. Theory. Geophys. J.R. Astron. Soc. **80**, 121–147, 1985

Hilterman, F.J.: Three-dimensional seismic modeling. Geophysics **35**(6), 1020–1037, 1970

Hutton, G.D.: The perfectly reflecting wedge used as a control model in seismic diffraction modelling. Geophys. Prosp. **35**, 681–699, 1987

Matthews, D.H., Cheadle, M.J.: Deep reflections from the Caledonides and Variscides west of Britain and comparison with the Himalayas. In: Reflection seismology: a global perspective. Barazangi, M., Brown, L., eds.: pp. 5–19. AGU Geodynamics series, Vol. 13, Washington D.C., 1986

Müller, G.: Earth-flattening approximation for body waves derived from geometric ray theory – improvements, corrections and range of applicability. J. Geophys. **42**, 429–436, 1977

Schilt, F.W., Kaufman, S., Long, G.H.: A three-dimensional study of seismic diffraction patterns from deep basement sources. Geophysics **46**(12), 1673–1683, 1981

Schneider, W.A.: Integral formulation for migration in two and three dimensions. Geophysics **43**, 49–76, 1978

Sen, K.S., Frazer, L.N.: Kirchhoff-Helmholtz reflection seismograms in a laterally inhomogeneous multi-layered elastic medium – II. Computations. Geoph. J.R. Astron. Soc. **82**, 415–437, 1985

Setto, I., Meissner, R.: Support of gravity modelling for seismic interpretation. Terra Cognita **6**, 346, 1986

Sullivan, M.F., Cohen, J.K.: Prestack Kirchhoff inversion of common-offset data. Geophysics **52**(6), 745–754, 1987
Temme, P.: A comparison of common-midpoint, single-shot, and plane wave depth migration. Geophysics **49**, 1896–1907, 1984
Trorey, A.W.: A simple theory for seismic diffractions. Geophysics **35**(5), 762–784, 1970
Trorey, A.W.: Diffractions for arbitrary source-receiver locations. Geophysics **42**(6), 1177–1182, 1977
Weber, K.: Variscan events: early Palaeozoic continental rift metamorphism and late Palaeozoic crustal shortening. In: Variscan tectonics of the North Atlantic region. Hutton, D.H.W., Sanderson, D.J., eds.: pp. 3–22. Special publication of the Geological Society. Oxford: Blackwell, 1984

Received September 8, 1987;
revised version November 2, 1987
Accepted November 4, 1987